CrossMark

ORIGINAL PAPER

# Physical properties and microstructures of La$_{1-x}$Pr$_x$PO$_4$ monazite-ceramics

Anja Thust[1] · Antje Hirsch[2] · Eiken Haussühl[1] · Nadine Schrodt[1] · Lise Loison[3] ·
Petra Schott[3] · Lars Peters[2] · Georg Roth[2] · Björn Winkler[1]

**Abstract** Synthetic La$_{1-x}$Pr$_x$PO$_4$ monazite-type powders
and ceramics with $0 \leq x \leq 1$ were analysed by scanning
electron microscopy, high-temperature powder X-ray diffrac-
tion, dilatometry, and plane wave ultrasound spectroscopy.
Ceramics were synthesised in a two-step sintering process
at 1273 and 1573 K. Final densities were up to 99.3% of the
theoretical densities. Each sample shows a homogeneous
distribution of grain sizes, which increase with increasing
sintering temperature. Grain sizes also depend on compo-
sition, with intermediate compositions yielding the largest
grains. In-situ high-temperature powder X-ray diffraction
shows that the volumetric thermal expansion coefficients of
the monazite powders decrease with increasing Pr content.
This behavior is not observed in dilatometry measurements
of the bulk samples (ceramics) because their thermal expan-
sion mainly depends on their density. Elastic properties show
the same dependence on the density.

✉ Antje Hirsch
hirsch@ifk.rwth-aachen.de

1 Institut für Geowissenschaften, Goethe-Universität,
Altenhöferallee 1, 60438 Frankfurt am Main, Germany

2 Institut für Kristallographie, RWTH Aachen University,
Jägerstraße 17–19, 52066 Aachen, Germany

3 Institut für Gesteinshüttenkunde, RWTH Aachen University,
Mauerstraße 5, 52064 Aachen, Germany

## Introduction

Polycrystalline ceramics are considered as potential waste
forms in geological repositories (Boatner et al. 1980; Mullica
et al. 1985; Ewing et al. 1995b; Ewing and Wang 2002). Natu-
ral monazites (LnPO$_4$) are typically crystalline (monoclinic,
$P2_1/n$), even though they often contain significant amounts
of radioactive elements such as Th and U (Ewing et al. 1995a;
Boatner and Sales 1988; Montel et al. 1996; Schlenz et al.
2013). The low recrystallisation temperature was reported to
be the main reason for this property. In addition to this high
radiation tolerance, monazite is known for its chemical stabil-
ity, crystal chemical flexibility, and high resistance to corro-
sion (Boatner et al. 1980; Sales et al. 1983; Weber et al. 1998;
Lumpkin 2006; Ewing 2007; Petek et al. 1981; Bregiroux et al.
2006). Compared to other waste forms such as borosilicate
glasses, monazite can be used for specific waste streams, such
as those dominated by the minor actinides (Boatner and Sales
1988; Schlenz et al. 2013; Lumpkin 2006; Weber et al. 2009).
The incorporation of these elements in the monazite structure
is restricted to defined lattice sites, yielding a durable matrix
for their stabilisation (Ewing and Wang 2002). Physical, ther-
mal, and microstructural properties influence the long-term
stability and integrity of ceramics. Monazite-type materials
have been studied extensively for several decades (Boatner
et al. 1980; Boatner and Sales 1988; Schlenz et al. 2013;
Weber et al. 1998, 2009; Lumpkin 2006; Ewing and Haaker
1980; Ewing 1999; Boatner 2002; Terra et al. 2006; Dacheux
et al. 2013a), but little systematic work has been presented on
solid solutions (Clavier et al. 2011, and references therein).
Recently, the solid solution series La$_{1-x}$Pr$_x$PO$_4$ was charac-
terised using various analysing techniques (Bauer et al. 2016;
Hirsch et al. 2017). In these studies, Pr$^{3+}$ served as a surrogate
for trivalent minor actinides. We used the powder samples
from Hirsch et al. (2017) to produce ceramics and analysed

their microstructure at different sintering steps. In addition, we compared the thermal expansion of the lattice parameters of these monazites obtained from in-situ high-temperature powder X-ray diffraction (HT-XRD) to thermal expansion of the ceramics obtained from dilatometry. Elastic properties of the ceramics were determined by plane wave/parallel plate ultrasound spectroscopy. The aim of this work is to obtain a better understanding of the behavior of monazite solid solution ceramics in terms of their microstructural, thermal, and physical properties with regards to the immobilisation of actinides.

## Materials and methods

### Synthesis and sample preparation

Powder samples of $La_{1-x}Pr_xPO_4$ ($\Delta x = 0.1$) were prepared by solid-state reaction similar to the method given by Bregiroux et al. (2007). The exact procedure is described elsewhere (Hirsch et al. 2017). To produce ceramic rods with Pr molar fractions of $x = 0;0.3;0.5;0.7;1$, fine powders were filled in rubber tubes and compacted. After evacuating the tubes, green pellets with a diameter of $\sim 6.5$ mm and lengths of $\sim 5$–12 mm were pressed isostatically at 60 MPa for 15 min at ambient temperatures. In a first step, the green pellets were sintered at 1273 K for 20 h. These incompletely densified samples will be named pre-ceramic. They were analysed by scanning electron microscopy (SEM) and dilatometry. Densities were calculated via measured mass and size of each sample. After a second sintering step at 1573 K for 15 h, the final ceramics were again analysed by SEM and dilatometry, and additionally by plane wave ultrasound spectroscopy. The density of the final ceramics was determined at ambient temperature via Archimedes' principle using water as immersion liquid. The pore volume fraction, $\phi$, was then calculated from the ratio of measured and theoretical density according to:

$$\Phi = \left(1 - \frac{\rho_{\text{measured}}}{\rho_{\text{theoretical}}}\right) \times 100. \tag{1}$$

The theoretical densities were calculated by the following:

$$\rho_{\text{theoretical}} = \frac{ZM}{VN_A}. \tag{2}$$

with $Z$ as the number of formula units per unit cell, $M$ as molecular weight in g/mol, $V$ as unit cell volume in $\text{Å}^3$ by Ni et al. (1995), and $N_A$ as the Avogadro number.

### Scanning electron microscopy

SEM was performed with a Phenom™ ProX desktop scanning electron microscope (LOT-QuantumDesign) equipped with a thermionic $CeB_6$ source and a high sensitivity multi-mode backscatter electron (BSE) detector. We used an

acceleration voltage of 10 kV for high-resolution imaging and 15 kV for energy dispersive X-ray spectroscopy (EDS) in low-vacuum mode. Samples were polished down manually using $Al_2O_3$ powders and then polished for about 15 min with 1 μm diamond paste followed by thermal etching for 4 h at 1273 K. High-resolution images were analysed using ImageJ (Rasband 1997) to obtain average grain size, grain size distribution, grain elongation, etc., by the method of best fitting ellipses. The SEM images (grey scale) were digitised in several steps to obtain a higher contrast, thereby highlighting the grain boundaries. The process of segmentation identifies individual grains, where black pixels represent the grains and white pixels the grain boundaries. For further details, see the ImageJ User guide (Rasband 1997). The average grain sizes were then compared to those determined by the lineal intercept method after Wurst and Nelson (1972). In this method, a set of lines is placed on a SEM image and the interceptions with the grain boundaries along these defined lines are counted. Using the following equation from Wurst and Nelson (1972):

$$d_{\text{grain}} = 1.56 \frac{l_{\text{line}}}{mN}. \tag{3}$$

the average grain size can be obtained, where $d_{\text{grain}}$ is the average grain size, $l_{\text{line}}$ is the total length of the used line, $N$ is the number of intercepts, and $m$ is the magnification. For further description of the proportionality constant, see Wurst and Nelson (1972).

### High-temperature X-ray diffraction

All samples were characterised at ambient conditions with powder X-ray diffraction (XRD) as described in Hirsch et al. (2017). Rietveld analyses (Rietveld 1967) were carried out using the program Topas Academic V 4.1 (Coelho 2000). A background polynomial, a modified Pseudo-Voigt profile function (Thompson et al. 1987), reflection asymmetry, sample height, lattice parameters, and fractional coordinates for all sites were refined. The structural model for $LaPO_4$ by Ni et al. (1995) was used for the refinements. Restraints for bond lengths and bond angles in the $PO_4$ tetrahedra and the $LnO_9$ polyhedra were introduced. Results of these refinements can be found in Hirsch et al. (2017).

In-situ HT-XRD was performed on a Bruker D8 Advanced DaVinci diffractometer in Bragg–Brentano $\theta$–$\theta$-geometry. The diffractometer was equipped with a Cu tube and a Ni filter, yielding a wavelength of 1.54060 Å. The data were collected using a Lynx Eye semiconductor strip detector. An Anton Paar HTK 2000 high-temperature chamber was used for the in-situ measurements. Samples ($x = 0, 0.2, 0.5, 0.8, 1$) were mixed with acetone and an internal $Al_2O_3$ standard. This mixture was dripped onto the Pt heating strip of the resistance furnace. Diffractograms were

taken in a $2\theta$ range of $10-80°$ with $\Delta2\theta = 0.03°$ and 19.2 s/step every 25 K while heating from 298 to 1373 K and every 50 K on cooling. At 298 and 1373 K, two measurements were carried out using 96 s/step. To obtain coefficients of thermal expansion (CTE), $\alpha$, the data were fitted with the expression:

$$a_i(T) = a_{i,0} + a_{i,0} \cdot \alpha\Delta T. \tag{4}$$

with

$$\alpha(T) = A + B(T - T_{ref}), \tag{5}$$

where $a_i(T)$ and $a_{i,0}$ are the lattice parameters $|\mathbf{a}|$, $|\mathbf{b}|$, $|\mathbf{c}|$, $\beta$ and the unit cell volume, at a temperature $T$ and at $T_{ref} = 1273$ K, respectively (Krishnan et al. 1979). $\Delta T = T - T_{ref}$ is the temperature change. $A$ and $B$ are fit parameters. To enable a comparison to the dilatometry data, normalised lengths and volume changes [i.e., deformation or strain after Haussühl (1983)] are defined as follows:

$$\frac{\Delta a_i}{a_{i,0}} = \frac{a_i(T) - a_{i,0}}{a_{i,0}}. \tag{6}$$

The volume-CTE was then divided by three to obtain an average coefficient.

## Dilatometry

Thermal expansion of the ceramics was measured in air with a push rod dilatometer (Netzsch DIL 402C) equipped with a high-temperature furnace (type 6.2191-26 from Netzsch). The dilatometer was calibrated using ceramic corundum rods. Cylindrical samples with lengths ranging from 4.724(4) to 12.288(8) mm were subjected to a single heating/cooling cycle from 305 up to 1373 K and back to room temperature with 2 K min⁻¹. CTE was obtained by fitting the deformation data using a third-order polynomial function after Haussühl (1983):

$$\frac{l - l_0}{l_0}(T) = W + X(T - T_{ref}) + Y(T - T_{ref})^2 + Z(T - T_{ref})^3 \tag{7}$$

with $T_{ref}$ as the reference temperature, $W$ as the intercept. $X$ is the linear, $Y$ is the quadratic, and $Z$ is the third-order thermal expansion coefficient, respectively. 1273 K was used as the reference temperature (Thust et al. 2015). On the basis of the corundum measurements, the accuracy is estimated to be 3%.

## Plane wave/parallel plate ultrasound spectroscopy

Plane wave/parallel plate ultrasound spectroscopy at ambient temperatures (293–296 K) was used to determine elastic coefficients of the final ceramics, as described by Arbeck et al. (2010). SEM measurements showed that all samples were isotropic and homogeneous; hence, no preferred orientation effects had to be accounted for. Employing an ultrasound transducer ($\alpha$-quartz with $x$- and $y$-cuts) driven by an impedance analyser (Agilent 4395A), ultrasound oscillations were excited to obtain resonance frequencies. To ensure acoustic coupling between sample and transducer, paraffin oil or resin was used. Taking into account the sample thickness ($d$) and the frequency difference between neighbouring resonant frequencies ($\Delta f$), sound velocities ($v$) were determined (Haussühl and Tillmanns 1997):

$$v = 2d(\Delta f). \tag{8}$$

Using sample densities ($\rho$), elastic stiffness coefficients ($c_{ij}$) were calculated (Yadawa et al. 2009):

$$c_{ij} = \rho v^2. \tag{9}$$

To obtain other mechanical properties in case of an elastically isotropic sample ($K$: bulk modulus, $G$: shear modulus; $\eta$: Poisson's ratio; $E$: Young's modulus), elastic longitudinal and shear coefficients ($c_{11}$ and $c_{44}$) were measured (Levy et al. 2001):

$$K = c_{11} - \frac{4}{3}c_{44} \tag{10}$$

$$G = c_{44} \tag{11}$$

$$\eta = \frac{3K - 2G}{6K + 2G} \tag{12}$$

$$E = 2G(1 + \eta). \tag{13}$$

## Results and discussion

### Microstructures

After the first sintering step, all pre-ceramics were extremely soft and fragile, while the final ceramics were fully densified and stable. Figure 1 shows the SEM micrographs of three samples in both states (pre-ceramics: a–c; final ceramics: d–f) and grain size distributions of the final ceramics (g–i). Since SEM photomicrographs of the pre-ceramics did not reveal enough details to apply the best fitting ellipses method (Heilbronner and Barrett 2013) using ImageJ (Rasband 1997), we focused on the intercept method (Wurst and Nelson 1972) to obtain average grain sizes (Fig. 2).

All analysed samples are homogeneous. Microstructure and grain shape of all pre-ceramics are similar and, within the experimental uncertainties, the average grain size does not vary with composition (Fig. 2). Final ceramics have larger grains (Figs. 1, 2). The grain growth of
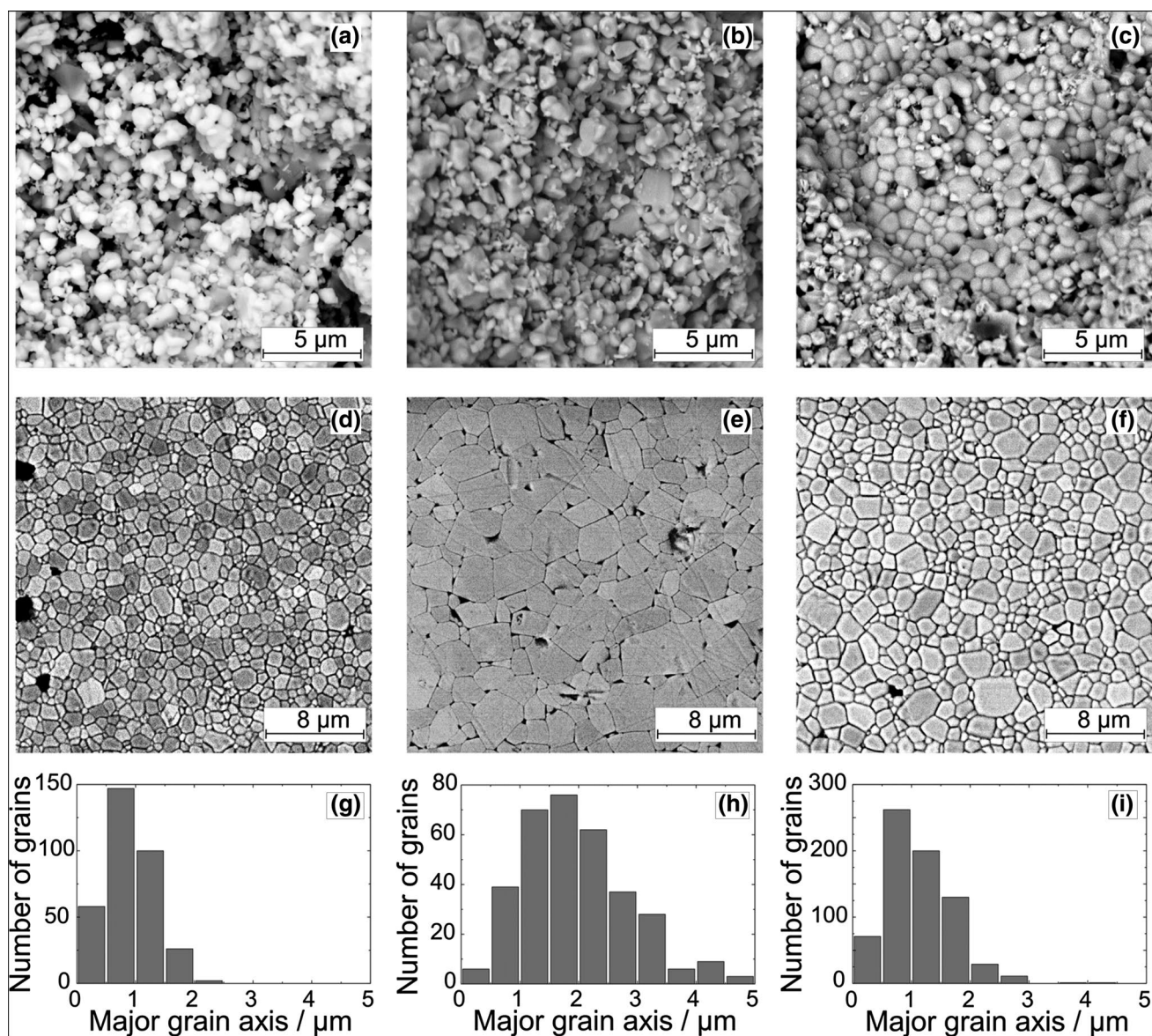
**Fig. 1** SEM micrographs and grain size distributions of $La_{1-x}Pr_xPO_4$ with $x = 0$ (a,d,g), $x = 0.5$ (b,e,h) and $x = 1$ (c,f,i). All pre-ceramics (**a**–**c**) show similar grain sizes, whereas intermediate final ceramics have larger grains (**e**) compared to end-members (**d**, **f**). Note that in contrast to **a**–**c**, Fig. **d**–**f** shows polished sections of corresponding ceramics. Scale bars are given. Grain size distributions of the final ceramics (**g**–**i**) highlight that intermediate compositions yield the largest grains

the end-members is slightly lower than that of intermediate compositions (Fig. 2). This might be due to enhanced sintering behavior of intermediate samples. However, this cannot be explained by a reduced melting temperature for the intermediate compositions in comparison to the end-members, which would result in a better sintering, since the melting temperature of theses intermediates is expected to be decreasing linearly from La ($2345 \pm 20$ K) to Pr ($2211 \pm 20$ K) (Hikichi and Nomura 1987). The observed grain growth can also not be attributed to the enthalpy of mixing studied by Hirsch et al. (2017), which is, within the

errors, similar for the end-members and the intermediate compositions. Average grain sizes calculated by the lineal intercept method (Wurst and Nelson 1972) seem to be slightly larger than those derived by the best fitting ellipses using ImageJ (Rasband 1997–2014). However, they are the same within the error. Within each sample, grain size, grain shape, and pore size are homogeneous. No local clustering of a specific grain size was observed (1). Low stability, in terms of low mechanical strength, of a repository matrix might cause fracturing and, therefore, enable water influx and corrosion. Consequently, pre-ceramics are not suitable
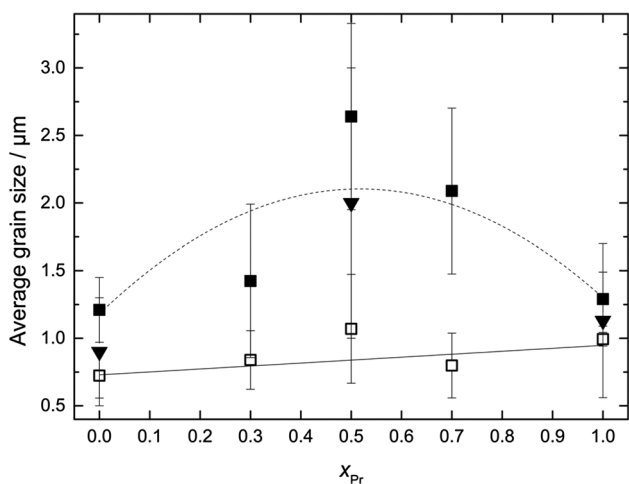
**Fig. 2** Average grain size of $La_{1-x}Pr_xPO_4$. Open squares represent grain sizes of the pre-ceramics determined using the intercept method (Wurst and Nelson 1972). Corresponding values for the *final ceramics* are depicted as filled squares. Filled triangles show grain sizes for the final ceramics determined using the best fitting ellipses (Heilbronner and Barrett 2013) (which was only possible for $x_{Pr} = 0, 0.5, 1$). While grain sizes for the pre-ceramics are independent of the composition, final ceramics of intermediate compositions seem to have larger grains than the end-members. Dashed and continuous lines are guides to the eye
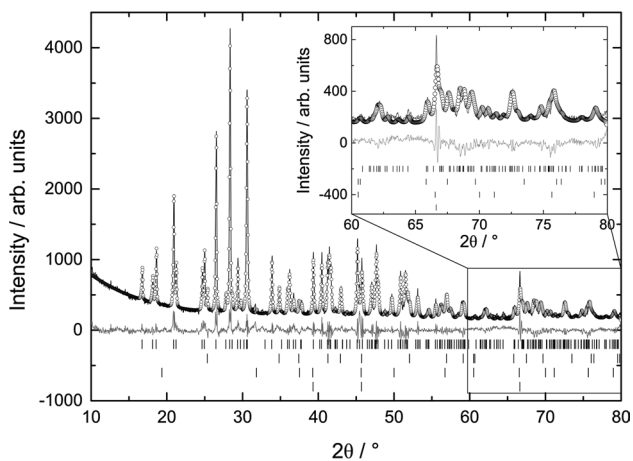


**Fig. 3** X-ray diffractogram of $LaPO_4$ at 1373 K: Measured intensity (open circles) is shown together with the refinement using the Rietveld method (black line) and the difference curve (grey line). Vertical tic marks indicate the position of calculated peaks for [top to bottom = monazite (Ni et al. 1995), $\alpha$-$Al_2O_3$ (Ishizawa et al. 1980), $\gamma$-$Al_2O_3$ (Zhou and Snyder 1991), and Pt (from the underlying heating strip) (Waseda et al. 1975)

to be used as a repository matrix due to their small grain sizes and their high porosity/low density. However, Perrière et al. (2007) showed that dense material with fine grain sizes exhibits maximal flexural strength. However, they also point out that pores essentially control fracture, because they are crucial defects for fracture.
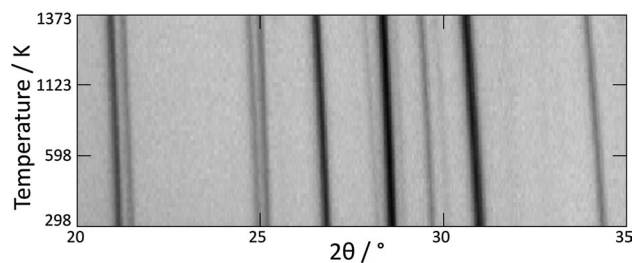


**Fig. 4** Two-dimensional film plot of the HT-diffraction data for $LaPO_4$ in the $2\theta$ range of $20°$–$35°$ during heating from 298 to 1373 K. Measurements were performed every 25 K. With increasing temperature, the peak positions shift towards smaller angles

**Table 1** Lattice parameters (**a**, **b**, **c**, and $\beta$) of the compositions $x = 0.0, 0.2, 0.5, 0.8, 1.0$ at temperature $T$ (298 K, 1373 K)

| $x_{Pr}$ | $T$/K | **a**/Å | **b**/Å | **c**/Å | $\beta$/° |
|---|---|---|---|---|---|
| 0.0 | 298 | 6.837(3) | 7.074(3) | 6.507(3) | 103.282(5) |
| | 1373 | 6.915(4) | 7.134(4) | 6.594(3) | 103.377(4) |
| 0.2 | 298 | 6.827(5) | 7.062(5) | 6.498(4) | 103.32(5) |
| | 1373 | 6.900(5) | 7.119(5) | 6.580(5) | 103.40(5) |
| 0.5 | 298 | 6.804(6) | 7.032(6) | 6.475(5) | 103.412(6) |
| | 1373 | 6.877(6) | 7.091(6) | 6.555(5) | 103.471(6) |
| 0.8 | 298 | 6.778(6) | 7.002(6) | 6.451(5) | 103.494(6) |
| | 1373 | 6.850(7) | 7.060(7) | 6.528(6) | 103.544(7) |
| 1.0 | 298 | 6.766(8) | 6.983(8) | 6.440(7) | 103.551(8) |
| | 1373 | 6.84(2) | 7.044(9) | 6.515(8) | 103.583(9) |
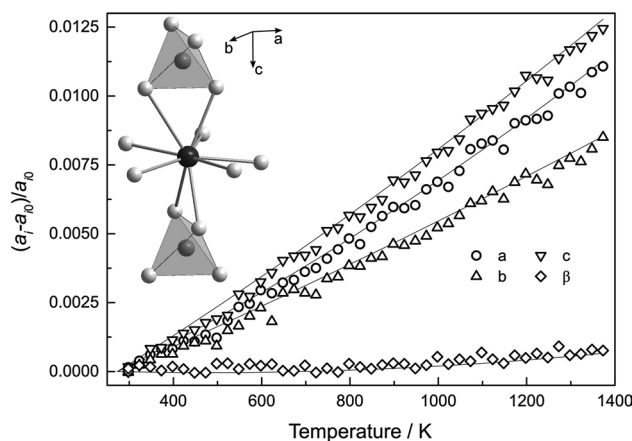


**Fig. 5** Temperature dependence of the normalised lattice parameters of $La_{0.5}Pr_{0.5}PO_4$. Error bars are smaller than the symbols. Solid lines correspond to third-order-polynomial fits. Lattice parameters increase monotonously with increasing temperature. The shortest axis $c$ shows the largest relative increase. Inset: chain structure of $LnO_9$ polyhedron and $PO_4$ tetrahedra along the $c$ axis (black: $Ln^{3+}$; grey: $P^{5+}$; white: $O^{2-}$; $PO_4$ tetrahedra indicated in grey)
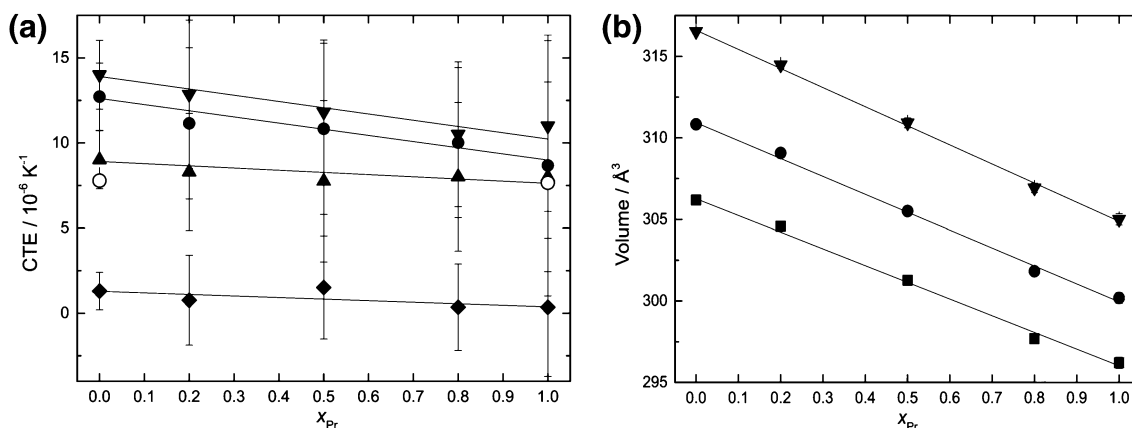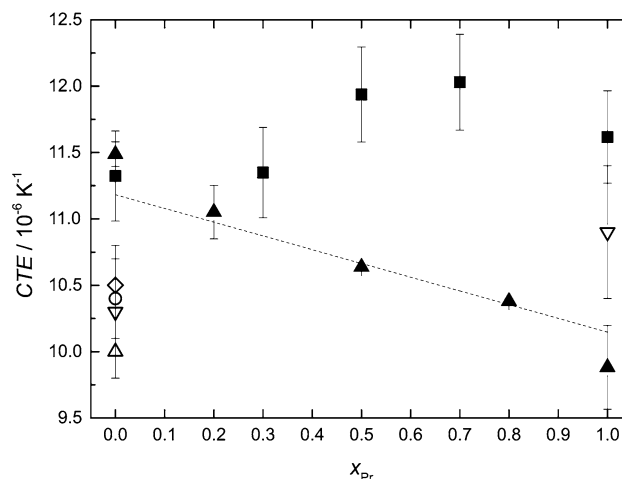
**Fig. 6** Left: Coefficients of thermal expansion (CTE) of the lattice parameters (filled symbols) as a function of the Pr content $x_{Pr}$: **a**: circles, **b**: up-pointing triangles, **c**: down-pointing triangles, $\beta$: diamonds. Open circles: calculated CTE for $LaPO_4$ and $PrPO_4$ from Li et al. (2009). Right: Unit cell volume vs. Pr content $x_{Pr}$ for the temperatures 298 K (squares), 823 K (circles) and 1373 K (triangles). In some cases, the error bars are smaller than the symbols. All lines are guides to the eye
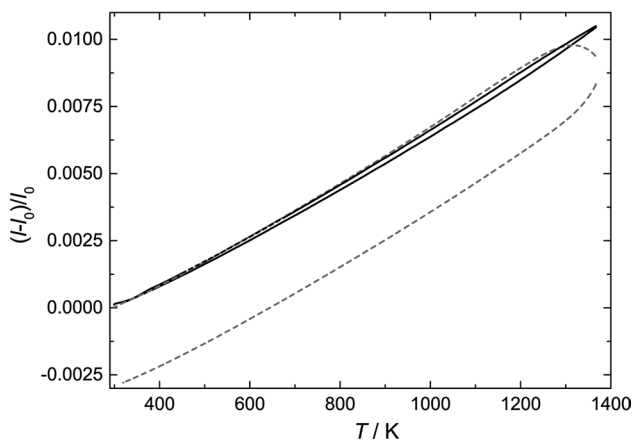


**Fig. 7** Deformation $(\frac{l-l_0}{l_0})$ of $La_{0.5}Pr_{0.5}PO_4$ measured using dilatometry while heating and cooling. While the pre-ceramic (dashed, grey line) shows a deviation between heating and cooling, the final ceramic (continuous, black line) remains almost unchanged

**Fig. 8** Linear thermal expansion coefficients (CTEs) of the powder samples (HT-XRD, filled triangles) and final ceramics (dilatometry, filled squares) of the solid solution $La_{1-x}Pr_xPO_4$ at 1273 K. In comparison: published data by Hikichi et al. (1997) (at 1273 K, open up-pointing triangle), Morgan and Marshall (1995) (at 1273 K, open diamond), Thust et al. (2015) (at 1273 K, open circle), and Perrière et al. (2007) (average value in the 473–1273 K temperature range, open down-pointing triangle). Dotted line: linear fit to the powder XRD data

## Thermal expansion by HT-XRD and dilatometry

All samples were single-phase monazite (Hirsch et al. 2017). Figure 3 shows the refinement of the powder X-ray experiment of $LaPO_4$ at 1373 K. The internal $Al_2O_3$ standard was not pure corundum at the beginning of the measurements but a mixture of $\alpha$-$Al_2O_3$ and $\gamma$-$Al_2O_3$. This was accounted for using corresponding structural models (Ishizawa et al. 1980; Zhou and Snyder 1991). The data quality was not sufficient to refine fractional coordinates without soft bond-length restraints. Hence, we restrict ourselves to discuss lattice parameters and volume changes only.

Figure 4 shows that with increasing temperature, peak positions shift towards smaller angles. That is due to the fact that the lattice parameters of all solid solution members increase monotonically by up to 3% with increasing temperature in the range studied here. This is shown in Fig. 5 for $x = 0.5$. Lattice parameters obtained from the two high-resolution measurements (at 298 and 1373 K) are given in Table 1. Results for all temperatures are given in the supporting electronic material.

**Fig. 9** Plane wave ultrasound resonance spectra of LaPO$_4$ for the determination of the elastic stiffness coefficients $c_{11}$ (ultrasound wave, left) and $c_{44}$ (shear wave, right). Insets: Frequency vs. number of the resonances used for the determination of the resonant frequencies ($\Delta f$)
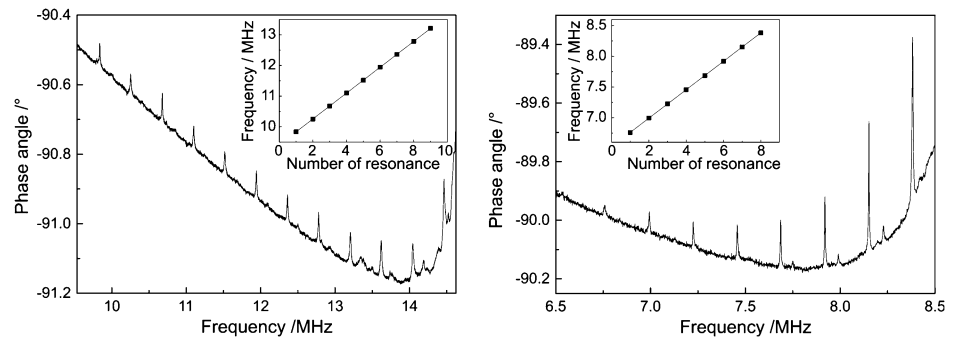


**Table 2** Sample properties and elastic stiffness coefficients of La$_{1-x}$Pr$_x$PO$_4$ solid solutions for pre-ceramics and final ceramics: sintering temperature $T$, density $\rho$, porosity $\Phi$ (for definition, see Eq. 1), sample thickness $d$, elastic stiffness coefficient $c_{ij}$ ($c_{11}$: longitudinal ultrasound wave, $c_{44}$: shear wave)

| $x$ | $T$ (K) | $\rho$ (g cm$^{-3}$) | $\Phi$ (%) | $d$ (mm) | $c_{11}$ (GPa) | $c_{44}$ (GPa) |
|---|---|---|---|---|---|---|
| *Pre-ceramics* | | | | | | |
| 0.0 | 1273 | 3.0(5) | 41(10) | 12.288(8) | – | – |
| 0.3 | 1273 | 2.9(2) | 43(4) | 8.525(11) | – | – |
| 0.5 | 1273 | 3.2(1) | 39(3) | 9.504(6) | – | – |
| 0.5 | 1273 | 3.2(1) | 39(1) | 9.616(15) | – | – |
| 0.7 | 1273 | 3.1(3) | 42(5) | 10.625(13) | – | – |
| 1.0 | 1273 | 3.4(3) | 36(6) | 6.918(1) | – | – |
| *Final ceramics* | | | | | | |
| 0.0 | 1573 | 5.015(6) | 1.3(1) | 6.955(2) | 172(1) | 52.3(4) |
| 0.3 | 1573 | 4.959(6) | 3.7(1) | 7.213(1) | 170(1) | 51.5(6) |
| 0.5 | 1573 | 5.106(6) | 1.7(1) | 5.315(3) | 186(1) | 54.6(4) |
| 0.5 | 1573 | 5.158(6) | 0.7(1) | 8.143(1) | 188(1) | 54.8(5) |
| 0.7 | 1573 | 5.104(6) | 2.6(1) | 7.619(2) | 182(1) | 53.7(5) |
| 1.0 | 1573 | 5.227(6) | 1.5(1) | 4.724(4) | 191(1) | 55.5(7) |

The **c**-axis shows the largest relative change, while **b** shows the smallest. This behavior is consistent with the elongation of the LnO$_9$-PO$_4$-chains in **c** direction being the main expansion mechanism, as was recently discussed by Asuvathraman and Kutty (2014). This chain structure is shown as an inset in Fig. 5.

For the individual lattice parameters for different compositions, no statistically significant difference in thermal expansion can be observed (Fig. 6, left). However, there seems to be a slight decrease in thermal volume expansion with increasing Pr content (Fig. 6, right).

Figure 7 exemplary shows the result of a dilatometric measurement. There is a clear deviation between heating and cooling run of the pre-ceramic. This is due to shrinkage of the sample upon grain growth. The final ceramic, however, remains almost unchanged, i.e., no further grain growth is taking place after the second sintering step.

The mean CTE at 1273 K of the powder samples and the CTE of the final ceramics are shown in Fig. 8. There is an obvious deviation of the CTE values between powder and ceramics. This might be due to the different reference temperatures used for the CTE calculation. CTE from HT-XRD

is calculated using the variation in the lattice parameters. In dilatometry, however, CTE is calculated from the length change of the ceramic samples. Therefore, the influence of the microstructure of the ceramics (e.g., grain boundaries, pores, and other defects) results in larger CTE (Li et al. 2009). This even masks the compositional differences observed in X-ray experiments. Microstructure and CTE values strongly depend on synthesis routes and conditions and are also affected by different sintering procedures. This could also explain the slight difference in CTE observed for the end-members studied here compared to the literature data (Hikichi et al. 1997; Morgan and Marshall 1995; Thust et al. 2015; Perrière et al. 2007).

## Elastic properties

Representative plane wave ultrasound resonance spectra of LaPO$_4$ are shown in Fig. 9. The elastic stiffness coefficients obtained from theses spectra of the final ceramics are $c_{11}$ (170–191 GPa) and $c_{44}$ (51.5–55.5 GPa) which are listed in Table 2. Pre-ceramics did not yield any ultrasound resonance signal due to their high porosity, which causes a significant
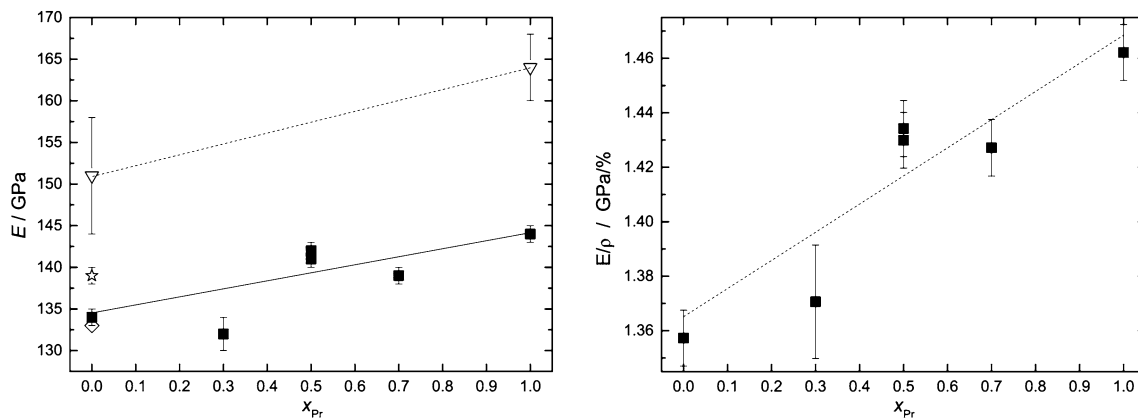
**Fig. 10** Left: Young's moduli $E$ of $La_{1-x}Pr_xPO_4$ calculated from $c_{11}$ and $c_{44}$ vs. composition: filled squares: this study; open diamonds: Morgan and Marshall (1995); open triangle: Perrière et al. (2007),

star: Thust et al. (2015). Right: Ratio of Young's moduli and relative densities vs. composition. Dashed line: fit to the data. The relative density is given as the percentage of theoretical density

dissipation of the ultrasound signal. The sample density $\rho$ and the corresponding porosity $\phi$ are also listed in Table 2.

The density of the final ceramics was up to 99.3% of the theoretical density using the structural model of Ni et al. (1995). The derived Young's moduli ($E$) are shown in Fig. 10 (left). As well as the thermal expansion and the density, Young's moduli of the final ceramics are also influenced by the microstructure. Due to the increasing theoretical density of monazites from La to Pr Ni et al. (1995), $E$ can be expected to increase. The observed $E$ (Fig. 10, right) values mainly reflect the actual ceramic density, which is a combination of theoretical density and microstructure. This explains the scatter of the data. Hence, $E$ can also be seen as a measure for the porosity of the sample and the sintering degree.

## Conclusions

In this study, we have presented new data for the microstructural, thermal, and physical properties of monazite-type solid solution ceramics, which are potential matrices for the immobilisation of actinides. Actinides behave very similar to lanthanides in monazite (e.g., Terra et al. 2003); therefore, the current study can help to predict properties of actinide-bearing monazites. According to Ewing and Weber (2010), it is possible to incorporate $Cm^{3+}$ and $Am^{3+}$ under oxidizing conditions. Several studies can be found on the direct substitution of actinides for lanthanides (e.g., Popa et al. 2007; Kitsay et al. 2004). Tetravalent actinides need to be incorporated via coupled substitution which may alter the chemical and physical behavior. However, microstructural and mechanical properties would have to be investigated on these specific materials as case studies for final disposal to

gain a precise understanding of the incorporation mechanisms of actinides (Ewing 2007).

We showed that a simple two-step sintering process without any special sintering program leads to homogeneous ceramic materials with high densities. Dacheux et al. (2013b) emphasize that this good response to sintering is an advantage for monazite as a nuclear waste form. Previously investigated ceramics of $(La,Eu)PO_4$ showed an increase of the CTE with increasing Eu content (Thust et al. 2015). This is not the case for Pr. While CTE from powder XRD decreases with increasing Pr content, the CTE for ceramics from dilatometry is also influenced by the microstructure. CTE and elastic properties depend on the actual sample density as shown by Thust et al. (2015) for $(La,Eu)PO_4$. Both properties, therefore, correlate with the degree of sintering. However, all data clearly show that the thermal behavior of $La_{1-x}Pr_xPO_4$ is comparable for powder and ceramics. This is consistent with the findings of Hirsch et al. (2017) that $La_{1-x}Pr_xPO_4$ forms an almost ideal solid solution.

## References

Arbeck D, Haussühl E, Bayarjagal L, Winkler B, Paulsen N, Haussühl S, Milman V (2010) Piezoelastic properties of retgersite determined by ultrasonic measurements. Eur Phys J B 73:167–175

Asuvathraman R, Kutty KVG (2014) Thermal expansion behaviour of a versatile monazite phase with simulated HLW: a high temperature X-ray diffraction study. Thermochim Acta 581:54–61

Bauer JD, Hirsch A, Bayarjargal L, Peters L, Roth G, Winkler B (2016) Schottky contribution to the heat capacity of monazite type (La, Pr)PO$_4$ from low temperature calorimetry and fluorescence measurements. Chem Phy Lett 654:97–102

Boatner LA (2002) Synthesis, structure, and properties of monazite, pretulite, and xenotime. Rev Mineral Geochem 48(1):87–121

Boatner LA, Beall GW, Abraham MM, Finch CB, Huray PG, and Rappaz M (1980) Monazite and other lanthanide orthophosphates as alternate actinide waste forms. In: Northrup CJM Jr. (ed) Mater Research Society proceedings, advances in nuclear science & technology, pp. 289 –296. Springer, US, (**ISBN 978-1-4684-3841-3**)

Boatner LA, Sales BC (1988) Monazite. In: Lutze W, Ewing RC (eds) Radioactive waste forms for the future. Elsevier Science Publishers Co., Inc., New York

Bregiroux D, Lucas S, Champion E, Audubert F, Bernache-Assollant D (2006) Sintering and microstructure of rare earth phosphate ceramics REPO$_4$ with RE = La, Ce or Y. J Eur Ceram Soc 26(3):279–287

Bregiroux D, Terra O, Audubert F, Dacheux N, Serin V, Podor R, Bernache-Assollant D (2007) Solid-state synthesis of monazite-type compounds containing tetravalent elements. Inorg Chem 46(24):10372–10382

Clavier N, Podor R, Dacheux N (2011) Crystal chemistry of the monazite structure. J Eur Ceram Soc 31:941–976

Coelho AA (2000) Topas v 2.0: general profile and structure analysis software for powder diffraction data. Bruker AXS, Karlsruhe

Dacheux N, Clavier N, Podor R (2013a) Monazite as a promising long-term radioactive waste matrix: benefits of high-structural flexibility and chemical durability. Am Mineral 98:833–847

Dacheux N, Clavier N, Podor R (2013b) Versatile monazite: resolving geological records and solving challenges in materials science: monazite as a promising long-term radioactive waste matrix: Benefits of high-structural flexibility and chemical durability. Am Mineral 98:833–847

Ewing RC (1999) Nuclear waste forms for actinides. Proc Natl Acad Sci USA 96(7):3432–3439

Ewing RC (2007) Ceramic matrices for plutonium disposition. Prog Nucl Energy 49(8):635–643

Ewing RC, Haaker RF (1980) The metamict state: implications for radiation damage in crystalline waste forms. Nucl Chem Waste Manag 1(1):51–57

Ewing RC, Wang L (2002) Phosphates as nuclear waste forms. Rev Mineral Geochem 48(1):673–699

Ewing RC, Weber WJ (2010) Actinide Waste Forms and Radiation Effects. In: Morss LR, Edelstein NM, Fuger J (eds) The Chemistry of the actinide and transactinide elements. Springer, Dordrecht

Ewing RC, Weber WJ, Clinard FW (1995a) Radiation effects in nuclear waste forms for high-level radioactive waste. Prog Nucl Energy 29(2):63–127

Ewing RC, Weber WJ, Jr Clinard FW (1995b) Radiation effects in nuclear waste forms for high-level radioactive waste. Prog Nucl Energy 29(2):127–63 (ISSN 0149-1970)

Haussühl E, Tillmanns E (1997) Physical properties and phase transitions of bis (guanidinium) zirconium bis (nitrilotriacetate) hydrate,[c (nh2) 3] 2zr [n (ch2coo) 3] 2zr h2o. Z Kristallogr 212:826–831

Haussühl Siegfried (1983) Kristallographie. Physik Verlag, Weinheim

Heilbronner R, Barrett S (2013) Image analysis in earth sciences: microstructures and textures of earth materials, vol 129. Springer Science & Business Media, Berlin

Hikichi Y, Hattori T (1987) Melting temperatures of monazite and xenotime. J Am Ceram Soc 70:C-252–C-253

Hikichi Y, Ota T, Hattori T (1997) Thermal, mechanical and chemical properties of sintered monazite-(La, Ce, Nd or Sm). Mineral J 19:123–130

Hirsch A, Kegler P, Alencar I, Ruiz-Fuertes J, Shelyug A, Peters L, Schreinemachers C, Neumann A, Neumeier S, Liermann H-P, Navrotsky A, Roth G (2017) Structural, vibrational, and thermochemical properties of the monazite-type solid solution La$_{1-x}$Pr$_x$PO$_4$. J Solid State Chem 245:82–88

Ishizawa N, Miyata T, Minato I, Marumo F, Iwai S (1980) A structural investigation of $\alpha$-Al$_2$O$_3$ at 2170 K. Acta Crystallogr B 36(2):228–230

Kitsay AA, Garbuzov VM, Burakov BE (2004) Synthesis of actinide-doped ceramics: from laboratory experiments to industrial scale technology. Sci Basis For Nucl Waste Manag Xxvii 807:237–242

Krishnan RS, Srinivasan R, Devanarayanan S (1979) Thermal Expansion of Crystals, vol 12. International Series in the Science of the solid state. Pergamon Press Ltd., Oxford

Levy M, Bass HE, Stern RR, Furr L, Keppens V (2001) Handbook of elastic properties of solids, liquids, and gases: elastic properties of solids: biological and organic materials, earth and marine sciences, vol 3. Academic Press, Cambridge

Li H, Zhang S, Zhou S, Cao X (2009) Bonding Characteristics, Thermal Expansibility, and Compressibility of RXO$_4$ (R = Rare Earths, X = P, As) within Monazite and Zircon Structures. Inorg Chem 48(10):4542–4548

Lumpkin GR (2006) Ceramic waste forms for actinides. Elements 2:365–372

Montel J-M, Foret S, Veschambre M, Nicollet C, Provost A (1996) Electron microprobe dating of monazite. Chem Geol 131:37–53

Morgan PED, Marshall DB (1995) Ceramic composites of monazite and alumina. J Am Ceram Soc 78:1553–1563

Mullica DF, Grossie DA, Boatner LA (1985) Structural refinements of praseodymium and neodymium orthophosphate. J Solid State Chem 58(1):71–77

Ni Y, Hughes JM, Mariano AN (1995) Crystal chemistry of the monazite and xenotime structures. Am Mineral 80(1):21–26

Perrière L, Bregiroux D, Naitali B, Audubert F, Champion E, Smith DS, Bernache-Assollant D (2007) Microstructural dependence of the thermal and mechanical properties of monazite LnPO$_4$ (Ln = La to Gd). J Eur Ceram Soc 27:3207–3213

Petek M, MAbraham MM, and Boatner LA (1981) Lanthanide orthophosphates as a matrix for solidified radioactive defense and reactor wastes. In: Symposium D Scientific Basis for Nuclear Waste Management IV, vol 6 of MRS Proceedings. Cambridge University Press, p181

Popa K, Colineau E, Wastin F, Konings RJM (2007) The low-temperature heat capacity of (Pu$_{0.1}$La$_{0.9}$)PO$_4$. Solid State Commun 144(1):74–77

Rasband WS (1997–2014) ImageJ.http://imagej.nih.gov/ij/. Accessed 25 Sept 2017

Rietveld HM (1967) Line profiles of neutron powder-diffraction peaks for structure refinement. Acta Crystallogr 22(1):151–152

Sales BC, White CW, Boatner LA (1983) A comparison of the corrosion characteristics of synthetic monazite and borosilicate glass containing simulated nuclear defense waste. Nucl Chem Waste Manag 4(4):281–289

Schlenz H, Heuser J, Neumann A, Schmitz S, Bosbach D (2013) Monazite as a suitable actinide waste form. Z Kristallogr 228:113–123

Terra O, Clavier N, Dacheux N, Podor R (2003) Preparation and characterization of lanthanum-gadolinium monazites as ceramics for radioactive waste storage. N J Chem 27(6):957–967

Terra O, Dacheux N, Audubert F, Podor R (2006) Immobilization of tetravalent actinides in phosphate ceramics. J Nucl Mater 352(1–3):224–232

Thompson P, Cox DE, Hastings JB (1987) Rietveld refinement of Debye-Scherrer synchrotron X-ray data from Al$_2$O$_3$. J Appl Crystallogr 20(2):79–83

Thust A, Arinicheva Y, Haussühl E, Ruiz-Fuertes J, Bayarjargal L, Vogel SC, Neumeier S, Winkler B (2015) Physical Properties of La$_{1-x}$Eu$_x$PO$_4$, $0 \leq x \leq 1$, Monazite-type ceramics. J Am Ceram Soc 98(12):4016–4021

Waseda Y, Hirata K, Ohtani M (1975) High-temperature thermal expansion of platinum, tantalum, molybdenum, and tungsten measured by X-ray diffraction. High Tem High Press 7(2):221–226

Weber WJ, Ewing RC, Catlow CRA, de la Rubia TD, Hobbs LW, Kinoshita C, Matzke H, Motta AT, Nastasi M, Salje EKH, Vance ER, Zinkle SJ (1998) Radiation effects in crystalline ceramics for the immobilization of high-level nuclear waste and plutonium. J Mater Res 13(06):1434–1484

Weber WJ, Navrotsky A, Stefanovsky S, Vance ER, Vernaz E (2009) Materials science of high-level nuclear waste immobilization. MRS Bull 34:46–53

Wurst JC, Nelson JA (1972) Lineal intercept technique for measuring grain size in two-phase polycrystalline ceramics. J Am Ceram Soc 55(2):109–109

Yadawa PK, Singh D, Pandey DK, Yadav RR (2009) Elastic and acoustic properties of heavy rare-earth metals. Open Acoust J 2:61–67

Zhou R-S, Snyder RL (1991) Structures and transformation mechanisms of the $\eta$, $\gamma$ and $\theta$ transition aluminas. Acta Crystallogr B 47(5):617–630